

Spontaneous ferromagnetism and finite surface energy gap in the topological insulator Bi_2Se_3 from surface Bi_{Se} antisite defects

Suhas Nahas,^{*} Biplab Sanyal,[†] and Annica M. Black-Schaffer[‡]

Department of Physics and Astronomy, Uppsala University, Box 516, SE-751 20 Uppsala, Sweden

(Dated: March 14, 2024)

We perform ab-initio calculations on Bi_{Se} antisite defects in the surface of Bi_2Se_3 , finding strong low-energy defect resonances with a spontaneous ferromagnetism, fixed to an out-of-plane orientation due to an exceptional large magnetic anisotropy energy. For antisite defects in the surface layer, we find semi-itinerant ferromagnetism and strong hybridization with the Dirac surface state, generating a finite energy gap. For deeper lying defects, such hybridization is largely absent, the magnetic moments becomes more localized, and no energy gap is present.

Topological insulators (TI) [1, 2] has been one of the most intensively studied areas in physics in the past decade, owing to their remarkable electronic properties: the bulk is insulating but the surfaces are metallic due to a gapless Dirac surface state (DSS) protected by time reversal symmetry (TRS).

Besides an interest in discovering new TIs, considerable effort has also been dedicated to opening up an energy gap in the DSS spectrum by breaking TRS, in order to enhance the electric control and also achieve the quantum anomalous Hall effect (QAHE)[3–5]. A natural route to break TRS is to introduce an effective magnetic field perpendicular to the surface of the TI [6]. Most of the studies along this route have involved doping the TI with magnetic impurities [6–15], whose magnetic moments might couple ferromagnetically through RKKY [16, 17], Van-Vleck [18], or other exchange [11, 12, 19–21] mechanisms to produce the necessary out-of-plane magnetic field. A more recent development has been the realization of intrinsic magnetism in MnBi_2Te_4 [22–25], where the Mn atoms order antiferromagnetically with an out-of-plane magnetic anisotropy.

However, for both magnetic impurities in TI and MnBi_2Te_4 , there seem to exist significant complications when it comes to opening a gap in the DSS, with experiments so far reporting both the presence of an energy gap [9, 26–29] and finite density of states [30–39] at the Dirac point. Also, in the case of thin films, the hybridization between the two DSSs could be the reason for a finite energy gap [40–42], and not TRS breaking. For magnetic impurities, a two-fluid description has been proposed [43] to account for the contradicting results. Here the DSS spectrum is indeed gapped due to TRS breaking, but at the same time the non-magnetic part of the scattering potential produces localized impurity-induced resonances [44–48] filling up the gap [49].

In this work, we show that a surface energy gap is generated in the most common TI, Bi_2Se_3 , from intrinsic Bi_{Se} antisite defects, entirely without the need of foreign magnetic atoms. By performing extensive ab-initio calculations of antisite defects, we find defect-induced low-energy resonances, which spontaneously acquire a

magnetic moment and thus gap the DSS. Antisite defects and their associated resonance states have already been observed experimentally using scanning tunneling microscopy (STM)[50–53], in both surface and subsurface layers, when growing Bi_2Se_3 in a Bi-rich environment [54–57]. An additional benefit of Bi_{Se} defects is that they behave as compensating p-type dopants, neutralizing the naturally occurring n-type Se vacancies by moving the Dirac point closer to the Fermi level [57, 58].

In detail, we show how Bi_{Se} antisite defects in the TI surface produce low-energy states, with a spontaneous magnetization which even increases for lower concentrations. We find a magnetic anisotropy energy favoring an out-of-plane magnetic orientation of individual antisite defects that is two orders of magnitude larger than for common magnetic dopants. Together with an appreciable ferromagnetic exchange coupling this guarantees an out-of-plane ferromagnetic alignment between different defects. For antisite defects in the surface layer, we find semi-itinerant ferromagnetism and defect states coupling strongly to the DSS, resulting in a sizable energy gap in the DSS. On the other hand, antisite defects in the first subsurface layer display more localized magnetism with no discernible hybridization with the DSSs and consequently no DSS energy gap. This also reveals that a significant hybridization is necessary between the DSS and the defect states for the magnetic moment to be able to produce an energy gap. Taken together, our results open up an entirely original and general pathway for designing magnetic and gapped TIs, by merely tuning the synthesizing conditions and thus completely avoiding the need for external magnetic impurity atoms.

Method.—We perform electronic structure calculations, based on density functional theory, as implemented in the Vienna Ab-initio Simulation Package (VASP [59]), on Bi_2Se_3 -slabs containing six quintuple layers ($\text{Se}_1\text{-Bi}_1\text{-Se}_2\text{-Bi}_2\text{-Se}_3$) in order to capture the TI surface, while still maintaining bulk conditions within the slab. On the surface we create a supercell by repeating the conventional surface unit cell, $n \times n$ ($n = 2, 3, 4$), adding one defect per supercell, resulting in defect concentrations $x \sim 25, 11, \text{ and } 6\%$. Below we mainly report re-

sults for antisite defects $\text{Bi}_{\text{Se}_{1,2}}$, i.e. Bi replacing either the surface Se_1 or subsurface Se_2 atom, see Fig. 1(a,b), but we also study Bi_{Se} defects in deeper layers, including the bulk. We carry out the structural and electronic optimizations using a plane-wave basis set with kinetic energy cut-off 270 eV [60], together with Projector Augmented Wave (PAW) pseudopotentials. We use the GGA for the exchange-correlation functional [61] and DFT-D3 [62] to properly account for the van der Waals corrections. Furthermore, we use a Γ -centered $k \times k \times 1$ grid to sample the Brillouin zone, where for even (odd) n we use $k \times n = 8(9)$ and $k \times n = 4(3)$ for the electronic and structural optimizations, respectively. We also use a 30 Å vacuum to isolate each periodic instance of the slab. In terms of convergence criteria, we use force and energy convergence thresholds of 10^{-6} eV (corresponding to 3×10^{-2} meV/Å) and 10^{-7} eV, respectively. We perform all calculations in a scalar relativistic manner, always including the effects of spin-orbit coupling, and also allow for a finite magnetization in all directions.

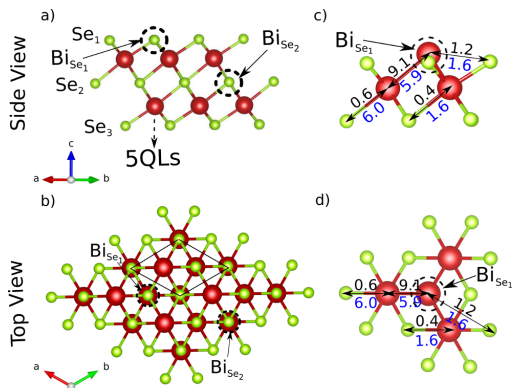


FIG. 1. Side (a) and top (b) views of the pristine Bi_2Se_3 slab, with Bi (Se) atoms in red (green) and the conventional lattice vectors of Bi_2Se_3 used as reference axes. Location of Bi_{Se_1} and Bi_{Se_2} antisite defects are indicated by dotted circles and surface unit-cell of pristine Bi_2Se_3 by black parallelogram. Side (c) and top (d) views of neighborhood of Bi_{Se_1} antisite defect with total relative (in %) bond length change in the presence (absence) of spin-orbit coupling in black (blue).

Structural distortions.—We start by performing structural optimizations of the atomic positions for each defected TI surface. This both establish the equilibrium positions of the Bi_{Se} defects and give a structural view on the impact of antisite defects. To quantify the latter, we track the atomic distortions caused by the Bi_{Se} defects by comparing with an equivalently relaxed pristine TI slab. In Fig. 1(c,d) we display in black text the relative change of bond lengths (in %) in the neighborhood of the Bi_{Se_1} defect, while blue text reports the equivalent change when ignoring spin-orbit coupling. As seen, the Bi_{Se_1} defect creates large local perturbations of the lattice structure, with bond lengths changing as much as

9% for nearest neighbor bonds. This is by all accounts a large structural change, which we at least partly can attribute to the 40% larger atomic size of the Bi atom compared to Se. In comparison, the next-nearest neighbor bonds show almost negligible distortion. If we were to ignore the spin-orbit coupling in the structural optimization we find that both the nearest and next-nearest neighbor bond show a similar change. This illustrates that spin-orbit coupling is essential to capture not just the DSS but also the correct atomic structure of antisite defects in TIs. We find similar structural patterns for the other antisite defects, including defects in the bulk of the TI, see Supplementary Material (SM) [63].

Magnetism.—We next turn to the electronic properties of antisite defects. Surprisingly we find that Bi_2Se_3 with antisite surface defects hosts a pronounced magnetization, despite the intrinsically non-magnetic nature of antisite defects. For both Bi_{Se_1} and Bi_{Se_2} , we observe a highly anisotropic, out-of-plane (c -direction), magnetization. Bi_{Se_3} (Bi on the third Se layer) also gives rise to a net magnetization, but the defect also easily migrates to the van der Waals gap during structural optimization. For antisite defects further into the bulk we find no magnetization. Interestingly, if we start with atomic structures optimized *without* spin-orbit coupling, we find no net magnetization for antisite defects in any layer, including $\text{Bi}_{\text{Se}_{1,2}}$. Thus, the large structural distortions caused by spin-orbit coupling is crucial for correctly determining the electronic ground state of antisite defects.

In Fig. 2(a) we show how the net magnetization varies as a function of defect concentration for the Bi_{Se_1} and Bi_{Se_2} defects. We find that both spin and orbital moments increase with decreasing concentration: the surface Bi_{Se_1} defect shows an almost three-fold increase in the spin magnetic moment when decreasing the defect concentration from 25% to 6% (see SM [63]), while the subsurface Bi_{Se_2} defect shows a minor increase. The increasing, and persistent, magnetization with decreasing defect concentrations assures that the magnetization is stable in the dilute defect limit. In Fig. 2(a) we also see that the orbital moments are large, strongly suggestive of a highly anisotropic magnetization [64–67]. In order to confirm this, we calculate magnetic anisotropy energy (MAE), i.e. the total energy difference between out-of-plane and in-plane magnetizations. Figure 2(b) shows how also the MAE increases significantly with decreasing defect concentration. Notably, the MAE is almost 20 (12) meV for the $\text{Bi}_{\text{Se}_{1(2)}}$ antisite defect at the lowest concentration. Such MAE values are impressive, about two orders of magnitude larger than what has been achieved in TIs with the magnetic transition metal impurities Cr, V or Mn, where the MAE is only of the order of 0.1 meV [68]. We also directly calculate the exchange coupling as the energy difference between ferromagnetic and anti-ferromagnetic c -axis alignments of two Bi_{Se_1} defects

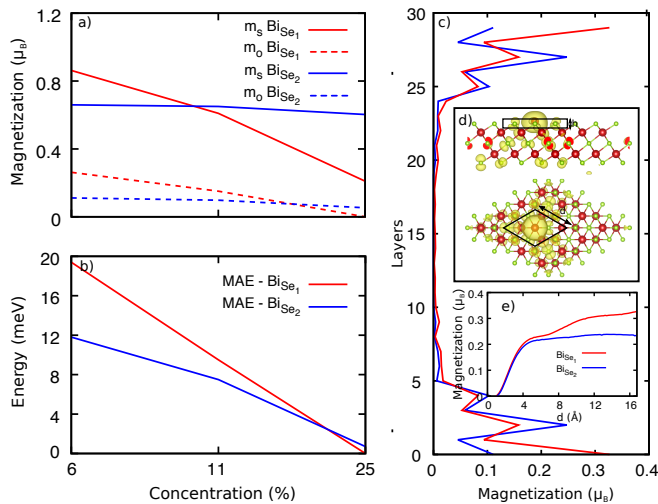


FIG. 2. (a) Magnetization, spin m_s (solid) and orbital m_o (dashed), and (b) MAE for BiSe_1 (red) and BiSe_2 (blue) antisite defects as a function of defect concentration. (c) Layer-resolved spin magnetization for each atomic layer for 6% BiSe_1 (red) and BiSe_2 (blue) antisite defects. (d) Real-space magnetization density in first surface layer for BiSe_1 defect with isovalue 0.1 times the maximum. (e) Integrated spin magnetization for BiSe_1 (red) and BiSe_2 (blue) defects over the volume of the black rhombus displayed in (d) (centered at the antisite defect with side d and thickness h), given as a function of d with h equal to the Bi-Se c -axis projected bond-length.

at a distance of ~ 14.5 Å and $\sim 6\%$ concentration, see SM [63]. We find the ferromagnetic configuration to be lower in energy by 3.6 meV. This is a large value considering the distance between the defects and contributes by a large amount (~ 500 meVÅ²) [69] to the spin-stiffness as predicted for spontaneous magnetization [70, 71]. Together with the large MAE, it also gives an exceptionally strong preference for an out-of-plane ferromagnetic alignment (with a large Curie temperature) of the antisite magnetic moments, thus creating optimal conditions for also opening a gap in the DSS [6, 72, 73].

To further understand the antisite-induced magnetic state, we analyze its spatial properties in the 6% $\text{BiSe}_{1,2}$ systems. In Fig. 2(c) we resolve the spin magnetic moments into layers of thickness h equal to the Bi-Se bond-length projected onto the c -axis, see black box in Fig. 2(d). We find that magnetism is only present in the surface layers, with a peak in the layer of the defect. For the in-plane behavior we show in Fig. 2(d) the real-space magnetization density of the surface atoms for the BiSe_1 defect. We find that the magnetization is semi-itinerant, extending with a three-fold spatial pattern from the defect to distances well beyond the primary unit-cell. To quantify the itinerancy, we study how the magnetization accumulates with distance away from the antisite defect. For this we plot in Fig. 2(e) the net

magnetization within a rhombus with the same shape as the unit-cell and with thickness h and centered around the antisite defect with varying side length d . For BiSe_1 the magnetization continuously increases with d , demonstrating semi-itinerancy. However, for the BiSe_2 defect we find that the magnetization is localized since a plateau develops when d equals about a quarter of the lattice parameter of the unit-cell in the a - b plane.

Surface energy gap.—Having established finite magnetism from intrinsically non-magnetic BiSe defects, we turn to investigating the electronic spectrum in detail. Since we find an exceptionally strong MAE, effectively guaranteeing an out-of-plane magnetic moment, we are particularly interested in how the magnetization affects the topologically protected DSSs in Bi_2Se_3 . In Fig. 3(a) we plot the band dispersion along the Γ -K direction for the BiSe_1 defect system at 6% concentration (blue) and compare it with the equivalent but defect-free system (red). To be able to effectively compare the two systems, we first set the Fermi level of the pristine slab to 0 eV at the Dirac point. We then align the spectrum of the defected slab such that the valence (VB) and conduction (CB) bands perfectly align for the defect and defect-free systems, see SM [63]. This is possible since both systems reach bulk conditions in the interior of the slabs. We refrain from plotting all bands belonging to the bulk but instead conceptually show their extent in the dark pink regions. We see a clear bulk band gap ranging from -0.05 eV to 0.27 eV (light pink), in agreement with previous predictions [74]. We also identify an intrinsic doping produced by the antisite defect, as the Fermi level (dotted lines) of the antisite defect system falls at a slightly higher energy (61 meV with 6% defects).

We next focus on the in-gap region, where we expect to find the DSS, but also defect states generated by the antisite defects. Initially we are interested only in the intrinsic DSSs, and therefore first exclude all bands belonging to the antisite defects. We can do this easily beyond the Γ point, as there the DSS and the antisite defect states have very different orbital and spatial characters: states belonging to the DSS is present throughout the surface, while the antisite defect states are heavily localized at the defect. At the Γ point we find finite hybridization between the DSS and some defect states, but, nonetheless, we can still remove the defect states based on their orbital weights and flat energy dispersion (due to their localization), see SM [63]. In this way we extract and plot only the DSSs for the BiSe_1 defect in Fig. 3(a). The DSS in the pristine system (red) and antisite system (blue) are very similar at higher energies, both showing a linear Dirac spectrum with the same slope. However, at low energies we find a clear 24 meV energy gap induced in the antisite system. The gap size at the Γ point is fully consistent with the slope of the DSS at higher energies. In Fig. 3(d) we plot the equivalent bands for the BiSe_2 defect, but here the DSS energy gap is negligible, despite

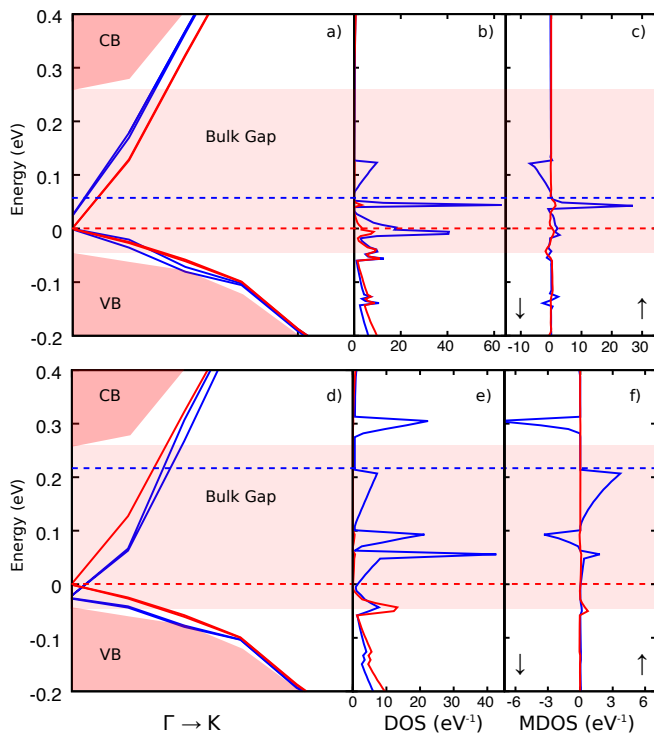


FIG. 3. (a,d) Band structure along $\Gamma - K$ for pristine (red) and BiSe_1 (a) and BiSe_2 (d) 6% defected (blue) TI system with defect states removed. Bulk conduction and valence bands (dark pink) are aligned to create a common bulk band gap (light pink), with the Fermi level (dotted lines) in pristine system set to 0 eV. (b,e) Complete density of states (DOS) and (c,f) magnetization density of states (MDOS) in the bulk (red) and the surface quintuple layer (blue) for the defected systems.

the finite magnetization. This is another property, along with the spatial extent of the magnetization, where we observe contrasting behavior for BiSe_1 and BiSe_2 defects.

Density of states.—To gain further insight into the magnetization and DSS energy gap we investigate the density of states (DOS). In Fig. 3(b,e) we compare the DOS in the bulk (red) with that of the surface quintuple layer of the BiSe_1 and BiSe_2 antisite systems (blue), respectively. By comparing these two DOS, we find that the DOS predominantly belonging to the $\text{BiSe}_{1(2)}$ antisite defect occupy an energy window ranging from around -20 (0) meV to 120 (220) meV, with respect to the pristine Dirac point, thus filling a large part of the bulk energy gap for both types of defects. However, we also observe that the defect states co-exist (in energy) with the induced energy gap for the BiSe_1 defect, while for the BiSe_2 defect, the defect states are mainly around 60 meV above the Dirac point of that defected system. By additionally studying the orbital character of all low-energy bands near the Γ -point, we find that the non-dispersive BiSe_1 states overlapping in energy with the Dirac point

strongly hybridizes with the DSS, see SM [63]. This hybridization explains why the BiSe_1 defect both generates a semi-itinerant magnetization and opens an energy gap in the DSS by effectively acting as a TRS breaking perturbation on the DSS. The strong hybridization between the magnetic BiSe_1 defect states and the DSS also provides the necessary pathway for a strong exchange coupling to align the antisite magnetic moments [75]. Here, with BiSe_e being an inherent defect, it naturally has the same (s,p) orbital character as the DSS. This provides an additional clear advantage, beyond the energy overlap, in generating a strong exchange coupling over transition metal atoms with their d orbital character [68].

The semi-itinerant magnetism and finite energy gap for the BiSe_1 system should be contrasted with the behavior of the BiSe_2 system. While the BiSe_2 defect states have a finite magnetization, they have a negligible overlap in energy with the DSS around its Dirac point. As a consequence, they do not effectively couple to the DSS and thus the magnetization stay localized and the energy gap in the DSS remains vanishingly small. Thus we conclude that a mere presence of an out-of-plane magnetic defect moments does not guarantee the opening up of an energy gap in TIs, but that an effective coupling between the magnetic defect states and the DSS needs to be present as well.

The creation of in-gap defect-induced resonance states for strong potential defects has previously been established for generic 2D Dirac materials [48], including the DSS in TIs [45] and also in the presence of finite magnetic moments [49]. Our ab-initio results establish that naturally occurring surface antisite BiSe_e defects act as such strong potential scatterers, inducing in-gap resonance states. This then also implies a so-called two-fluid behavior [43], with both the dispersive DSS and the localized impurity resonance states filling the TI bulk energy gap, as is clearly visible in Fig. 3.

Finally, we compare the magnetization density of states (MDOS) between the bulk and surface in Fig. 3(c,f) for the $\text{BiSe}_{1,2}$ defects. We find that the magnetization in the system is almost exclusively associated with the in-gap defect states. This also finally offers an explanation as to why the antisite defect states spontaneously become magnetized in the first place: the defect resonance states generate a large DOS at the Fermi level $\rho(E_F)$, which necessarily becomes prone to spontaneous magnetization. In its simplest incarnation the instability towards magnetism is given by a Stoner-like criterion $\rho(E_F)U > 1$, where U is the electron-electron interaction strength [76]. Our ab-initio results on antisite BiSe_e defects on the surface of the TI Bi_2Se_3 show that antisite defects are indeed strong enough potential scatterers to generate these low-energy defect-induced resonances, which then thanks to finite exchange interactions in the TI also become spontaneously magnetized, see SM for further information [63]. Moreover, naturally occurring

Se vacancy states will not be detrimental as they appear at a larger energy [52, 77]

Conclusions.—Our fully relativistic ab-initio calculations show that intrinsic antisite Bi_{Se} defects in the surface layer of the TI Bi₂Se₃ generates a finite energy gap in the topologically protected DSSs. The antisite defect produces low-energy resonance states, which spontaneously become magnetic with an exceptionally large MAE guaranteeing an out-of-plane magnetic moment. With the defect states also overlapping in energy with the Dirac point, they hybridize with the DSS and thus the surface antisite defect acts as an effective magnetic field opening an energy gap in the DSS. For antisite defects buried in the first subsurface layer we also find a finite magnetization, but the overlap with the DSS is negligible and thus no measurable energy gap is present in the DSS. These results illustrates both that naturally occurring defects can produce a magnetic TI and that magnetic defect moments require effective coupling to the DSS to open an energy gap. Moreover, the results provide an important observation on the site dependence of defects in exhibiting essential physics of TIs.

We thank A. Bouhon, X. Chen, R. Esteban-Puyuelo, B. Ghosh, M. Mashkooi, F. Parhizgar, and D. Wang for fruitful discussions. This work was supported by the Swedish Research Council (Vetenskapsrådet, Grant Nos. 2014-3721 and 2018-03488), the Swedish Foundation for Strategic Research (SSF), and the Wallenberg Academy Fellows program through the Knut and Alice Wallenberg Foundation. The simulations were performed on resources provided by the Swedish National Infrastructure for Computing (SNIC) at HPC2N, NSC, PDC, and UPPMAX.

* suhas.nahas@physics.uu.se

† biplab.sanyal@physics.uu.se

‡ annica.black-schaffer@physics.uu.se

- [1] M. Z. Hasan and C. L. Kane, *Rev. Mod. Phys.* **82**, 3045 (2010)
- [2] X.-L. Qi and S.-C. Zhang, *Rev. Mod. Phys.* **83**, 1057 (2011)
- [3] F. D. M. Haldane, *Phys. Rev. Lett.* **61**, 2015 (1988)
- [4] M. Onoda and N. Nagaosa, *Phys. Rev. Lett.* **90**, 206601 (2003)
- [5] C.-X. Liu, X.-L. Qi, X. Dai, Z. Fang, and S.-C. Zhang, *Phys. Rev. Lett.* **101**, 146802 (2008)
- [6] Y. Tokura, K. Yasuda, and A. Tsukazaki, *Nat. Rev. Phys.* **1**, 126 (2019)
- [7] Y. S. Hor, P. Roushan, H. Beidenkopf, J. Seo, D. Qu, J. G. Checkelsky, L. A. Wray, D. Hsieh, Y. Xia, S.-Y. Xu, D. Qian, M. Z. Hasan, N. P. Ong, A. Yazdani, and R. J. Cava, *Phys. Rev. B* **81**, 195203 (2010)
- [8] R. Yu, W. Zhang, H.-J. Zhang, S.-C. Zhang, X. Dai, and Z. Fang, *Science* **329**, 61 (2010)
- [9] C.-Z. Chang, J. Zhang, X. Feng, J. Shen, Z. Zhang, M. Guo, K. Li, Y. Ou, P. Wei, L.-L. Wang, Z.-Q. Ji, Y. Feng, S. Ji, X. Chen, J. Jia, X. Dai, Z. Fang, S.-C. Zhang, K. He, Y. Wang, L. Lu, X.-C. Ma, and Q.-K. Xue, *Science* **340**, 167 (2013)
- [10] C.-Z. Chang, W. Zhao, D. Y. Kim, H. Zhang, B. A. Assaf, D. Heiman, S.-C. Zhang, C. Liu, M. H. W. Chan, and J. S. Moodera, *Nat. Mater.* **14**, 473 (2015)
- [11] T. R. F. Peixoto, H. Bentmann, S. Schreyeck, M. Winnerlein, C. Seibel, H. Maaß, M. Al-Baidhani, K. Treiber, S. Schatz, S. Grauer, C. Gould, K. Brunner, A. Ernst, L. W. Molenkamp, and F. Reinert, *Phys. Rev. B* **94**, 195140 (2016)
- [12] W. Zhang, D. West, S. H. Lee, Y. Qiu, C.-Z. Chang, J. S. Moodera, Y. S. Hor, S. Zhang, and W. Wu, *Phys. Rev. B* **98**, 115165 (2018)
- [13] W. Liu, Y. Xu, L. He, G. van der Laan, R. Zhang, and K. Wang, *Sci. Adv.* **5** (2019)
- [14] A. J. Bestwick, E. J. Fox, X. Kou, L. Pan, K. L. Wang, and D. Goldhaber-Gordon, *Phys. Rev. Lett.* **114**, 187201 (2015)
- [15] X. Kou, S.-T. Guo, Y. Fan, L. Pan, M. Lang, Y. Jiang, Q. Shao, T. Nie, K. Murata, J. Tang, Y. Wang, L. He, T.-K. Lee, W.-L. Lee, and K. L. Wang, *Phys. Rev. Lett.* **113**, 137201 (2014)
- [16] D. A. Abanin and D. A. Pesin, *Phys. Rev. Lett.* **106**, 136802 (2011)
- [17] J.-J. Zhu, D.-X. Yao, S.-C. Zhang, and K. Chang, *Phys. Rev. Lett.* **106**, 097201 (2011)
- [18] M. Li, C.-Z. Chang, L. Wu, J. Tao, W. Zhao, M. H. W. Chan, J. S. Moodera, J. Li, and Y. Zhu, *Phys. Rev. Lett.* **114**, 146802 (2015)
- [19] M. G. Vergniory, M. M. Otrokov, D. Thonig, M. Hoffmann, I. V. Maznichenko, M. Geilhufe, X. Zubizarreta, S. Ostanin, A. Marmodoro, J. Henk, W. Hergert, I. Mertig, E. V. Chulkov, and A. Ernst, *Phys. Rev. B* **89**, 165202 (2014)
- [20] M. Ye, T. Xu, G. Li, S. Qiao, Y. Takeda, Y. Saitoh, S.-Y. Zhu, M. Nurmatamat, K. Sumida, Y. Ishida, S. Shin, and A. Kimura, *Phys. Rev. B* **99**, 144413 (2019)
- [21] A. Tcakaev, V. B. Zabolotnyy, R. J. Green, T. R. F. Peixoto, F. Stier, M. Dettbarn, S. Schreyeck, M. Winnerlein, R. C. Vidal, S. Schatz, H. B. Vasili, M. Valvidares, K. Brunner, C. Gould, H. Bentmann, F. Reinert, L. W. Molenkamp, and V. Hinkov, *Phys. Rev. B* **101**, 045127 (2020)
- [22] J. Li, Y. Li, S. Du, Z. Wang, B.-L. Gu, S.-C. Zhang, K. He, W. Duan, and Y. Xu, *Sci. Adv.* **5** (2019)
- [23] D. Zhang, M. Shi, T. Zhu, D. Xing, H. Zhang, and J. Wang, *Phys. Rev. Lett.* **122**, 206401 (2019)
- [24] A. Zeugner, F. Nietschke, A. U. B. Wolter, S. Gaß, R. C. Vidal, T. R. F. Peixoto, D. Pohl, C. Damm, A. Lubk, R. Hentrich, S. K. Moser, C. Fornari, C. H. Min, S. Schatz, K. Kißner, M. Ünzelmann, M. Kaiser, F. Scaravaggi, B. Rellinghaus, K. Nielsch, C. Hess, B. Büchner, F. Reinert, H. Bentmann, O. Oeckler, T. Doert, M. Ruck, and A. Isaeva, *Chem. Mater.* **31**, 2795 (2019)
- [25] Y. Gong, J. Guo, J. Li, K. Zhu, M. Liao, X. Liu, Q. Zhang, L. Gu, L. Tang, X. Feng, D. Zhang, W. Li, C. Song, L. Wang, P. Yu, X. Chen, Y. Wang, H. Yao, W. Duan, Y. Xu, S.-C. Zhang, X. Ma, Q.-K. Xue, and K. He, *Chin. Phys. Lett.* **36**, 076801 (2019)
- [26] J. Sánchez-Barriga, A. Varykhalov, G. Springholz, H. Steiner, R. Kirchschrager, G. Bauer, O. Caha, E. Schierle, E. Weschke, A. A. Únal, S. Valencia, M. Dunst, J. Braun, H. Ebert, J. Minár, E. Golias, L. V.

- Yashina, A. Ney, V. Holý, and O. Rader, *Nat. Commun.* **7**, 10559 (2016)
- [27] M. M. Otrokov, I. I. Klimovskikh, H. Bentmann, D. Estyunin, A. Zeugner, Z. S. Aliev, S. Gaß, A. U. B. Wolter, A. V. Koroleva, A. M. Shikin, M. Blanco-Rey, M. Hoffmann, I. P. Rusinov, A. Y. Vyazovskaya, S. V. Ereemeev, Y. M. Koroteev, V. M. Kuznetsov, F. Freyse, J. Sánchez-Barriga, I. R. Amiraslanov, M. B. Babanly, N. T. Mamedov, N. A. Abdullayev, V. N. Zverev, A. Alfonso, V. Kataev, B. Büchner, E. F. Schwier, S. Kumar, A. Kimura, L. Petaccia, G. Di Santo, R. C. Vidal, S. Schatz, K. Kißner, M. Ünzelmann, C. H. Min, S. Moser, T. R. F. Peixoto, F. Reinert, A. Ernst, P. M. Echenique, A. Isaeva, and E. V. Chulkov, *Nature* **576**, 416 (2019)
- [28] Y. L. Chen, J.-H. Chu, J. G. Analytis, Z. K. Liu, K. Igarashi, H.-H. Kuo, X. L. Qi, S. K. Mo, R. G. Moore, D. H. Lu, M. Hashimoto, T. Sasagawa, S. C. Zhang, I. R. Fisher, Z. Hussain, and Z. X. Shen, *Science* **329**, 659 (2010)
- [29] L. A. Wray, S.-Y. Xu, Y. Xia, D. Hsieh, A. V. Fedorov, Y. S. Hor, R. J. Cava, A. Bansil, H. Lin, and M. Z. Hasan, *Nat. Phys.* **7**, 32 (2011)
- [30] T. Valla, Z.-H. Pan, D. Gardner, Y. S. Lee, and S. Chu, *Phys. Rev. Lett.* **108**, 117601 (2012)
- [31] M. R. Scholz, J. Sánchez-Barriga, D. Marchenko, A. Varykhalov, A. Volykhov, L. V. Yashina, and O. Rader, *Phys. Rev. Lett.* **108**, 256810 (2012)
- [32] H. Li, S.-Y. Gao, S.-F. Duan, Y.-F. Xu, K.-J. Zhu, S.-J. Tian, J.-C. Gao, W.-H. Fan, Z.-C. Rao, J.-R. Huang, J.-J. Li, D.-Y. Yan, Z.-T. Liu, W.-L. Liu, Y.-B. Huang, Y.-L. Li, Y. Liu, G.-B. Zhang, P. Zhang, T. Kondo, S. Shin, H.-C. Lei, Y.-G. Shi, W.-T. Zhang, H.-M. Weng, T. Qian, and H. Ding, *Phys. Rev. X* **9**, 041039 (2019)
- [33] Y.-J. Hao, P. Liu, Y. Feng, X.-M. Ma, E. F. Schwier, M. Arita, S. Kumar, C. Hu, R. Lu, M. Zeng, Y. Wang, Z. Hao, H.-Y. Sun, K. Zhang, J. Mei, N. Ni, L. Wu, K. Shimada, C. Chen, Q. Liu, and C. Liu, *Phys. Rev. X* **9**, 041038 (2019)
- [34] Y. J. Chen, L. X. Xu, J. H. Li, Y. W. Li, H. Y. Wang, C. F. Zhang, H. Li, Y. Wu, A. J. Liang, C. Chen, S. W. Jung, C. Cacho, Y. H. Mao, S. Liu, M. X. Wang, Y. F. Guo, Y. Xu, Z. K. Liu, L. X. Yang, and Y. L. Chen, *Phys. Rev. X* **9**, 041040 (2019)
- [35] T. Schlenk, M. Bianchi, M. Koleini, A. Eich, O. Pietzsch, T. O. Wehling, T. Frauenheim, A. Balatsky, J.-L. Mi, B. B. Iversen, J. Wiebe, A. A. Khajetoorians, P. Hofmann, and R. Wiesendanger, *Phys. Rev. Lett.* **110**, 126804 (2013)
- [36] H. Beidenkopf, P. Roushan, J. Seo, L. Gorman, I. Drozdov, Y. S. Hor, R. J. Cava, and A. Yazdani, *Nat. Phys.* **7**, 939 (2011)
- [37] P. Sessi, F. Reis, T. Bathon, K. A. Kokh, O. E. Tereshchenko, and M. Bode, *Nat. Commun.* **5**, 5349 (2014)
- [38] F. Yang, Y. R. Song, H. Li, K. F. Zhang, X. Yao, C. Liu, D. Qian, C. L. Gao, and J.-F. Jia, *Phys. Rev. Lett.* **111**, 176802 (2013)
- [39] Y. Okada, C. Dhital, W. Zhou, E. D. Huemiller, H. Lin, S. Basak, A. Bansil, Y.-B. Huang, H. Ding, Z. Wang, S. D. Wilson, and V. Madhavan, *Phys. Rev. Lett.* **106**, 206805 (2011)
- [40] J. Linder, T. Yokoyama, and A. Sudbø, *Phys. Rev. B* **80**, 205401 (2009)
- [41] H.-Z. Lu, W.-Y. Shan, W. Yao, Q. Niu, and S.-Q. Shen, *Phys. Rev. B* **81**, 115407 (2010)
- [42] C.-X. Liu, H. J. Zhang, B. Yan, X.-L. Qi, T. Frauenheim, X. Dai, Z. Fang, and S.-C. Zhang, *Phys. Rev. B* **81**, 041307(R) (2010)
- [43] P. Sessi, R. R. Biswas, T. Bathon, O. Storz, S. Wilfert, A. Barla, K. A. Kokh, O. E. Tereshchenko, K. Fauth, M. Bode, and A. V. Balatsky, *Nat. Commun.* **7**, 12027 (2016)
- [44] R. R. Biswas and A. V. Balatsky, *Phys. Rev. B* **81**, 233405 (2010)
- [45] A. M. Black-Schaffer and A. V. Balatsky, *Phys. Rev. B* **85**, 121103(R) (2012)
- [46] A. M. Black-Schaffer and A. V. Balatsky, *Phys. Rev. B* **86**, 115433 (2012)
- [47] Z. Alpichshev, R. R. Biswas, A. V. Balatsky, J. G. Analytis, J.-H. Chu, I. R. Fisher, and A. Kapitulnik, *Phys. Rev. Lett.* **108**, 206402 (2012)
- [48] T. Wehling, A. Black-Schaffer, and A. Balatsky, *Adv. Phys.* **63**, 1 (2014)
- [49] A. M. Black-Schaffer, A. V. Balatsky, and J. Fransson, *Phys. Rev. B* **91**, 201411(R) (2015)
- [50] S. Urazhdin, D. Bilc, S. H. Tessmer, S. D. Mahanti, T. Kyratsi, and M. G. Kanatzidis, *Phys. Rev. B* **66**, 161306(R) (2002)
- [51] S. Kim, M. Ye, K. Kuroda, Y. Yamada, E. E. Krasovskii, E. V. Chulkov, K. Miyamoto, M. Nakatake, T. Okuda, Y. Ueda, K. Shimada, H. Namatame, M. Taniguchi, and A. Kimura, *Phys. Rev. Lett.* **107**, 056803 (2011)
- [52] C. Mann, D. West, I. Miotkowski, Y. P. Chen, S. Zhang, and C.-K. Shih, *Nat. Commun.* **4**, 2277 (2013)
- [53] J. Dai, D. West, X. Wang, Y. Wang, D. Kwok, S.-W. Cheong, S. B. Zhang, and W. Wu, *Phys. Rev. Lett.* **117**, 106401 (2016)
- [54] J.-M. Zhang, W. Zhu, Y. Zhang, D. Xiao, and Y. Yao, *Phys. Rev. Lett.* **109**, 266405 (2012)
- [55] D. West, Y. Y. Sun, H. Wang, J. Bang, and S. B. Zhang, *Phys. Rev. B* **86**, 121201(R) (2012)
- [56] D. O. Scanlon, P. D. C. King, R. P. Singh, A. de la Torre, S. M. Walker, G. Balakrishnan, F. Baumberger, and C. R. A. Catlow, *Adv. Mater.* **24**, 2154 (2012)
- [57] L. Xue, P. Zhou, C. X. Zhang, C. Y. He, G. L. Hao, L. Z. Sun, and J. X. Zhong, *AIP Adv.* **3**, 052105 (2013)
- [58] Y. S. Hor, A. Richardella, P. Roushan, Y. Xia, J. G. Checkelsky, A. Yazdani, M. Z. Hasan, N. P. Ong, and R. J. Cava, *Phys. Rev. B* **79**, 195208 (2009)
- [59] G. Kresse and J. Furthmüller, *Phys. Rev. B* **54**, 11169 (1996)
- [60] We have checked that increasing the kinetic energy cut-off to 600 eV does not change the results for the 11% Bi_{Se1,2} defect
- [61] K. Shirali, W. A. Shelton, and I. Vekhter, “Importance of van der waals interactions for ab initio studies of topological insulators,” (2019), [arXiv:1905.01269](https://arxiv.org/abs/1905.01269) [cond-mat.mes-hall]
- [62] S. Grimme, J. Antony, S. Ehrlich, and H. Krieg, *J. Chem. Phys.* **132**, 154104 (2010)
- [63] See *Supplementary Material for more information.*
- [64] P. Bruno, *Phys. Rev. B* **39**, 865 (1989)
- [65] R. Skomski, A. Kashyap, and A. Enders, *J. Appl. Phys.* **109**, 07E143 (2011)
- [66] I. G. Rau, S. Baumann, S. Rusponi, F. Donati, S. Stepanow, L. Gragnaniello, J. Dreiser, C. Piamonteze, F. Nolting, S. Gangopadhyay, O. R. Albertini, R. M.

- Macfarlane, C. P. Lutz, B. A. Jones, P. Gambardella, A. J. Heinrich, and H. Brune, *Science* **344**, 988 (2014)
- [67] X. Ou, H. Wang, F. Fan, Z. Li, and H. Wu, *Phys. Rev. Lett.* **115**, 257201 (2015)
- [68] M. F. Islam, C. M. Canali, A. Pertsova, A. Balatsky, S. K. Mahatha, C. Carbone, A. Barla, K. A. Kokh, O. E. Tereshchenko, E. Jiménez, N. B. Brookes, P. Gargiani, M. Valvidares, S. Schatz, T. R. F. Peixoto, H. Bentmann, F. Reinert, J. Jung, T. Bathon, K. Fauth, M. Bode, and P. Sessi, *Phys. Rev. B* **97**, 155429 (2018)
- [69] M. Pajda, J. Kudrnovský, I. Turek, V. Drchal, and P. Bruno, *Phys. Rev. B* **64**, 174402 (2001)
- [70] D. M. Edwards and M. I. Katsnelson, *J. Phys. Condens. Matter* **18**, 7209 (2006)
- [71] O. V. Yazyev and M. I. Katsnelson, *Phys. Rev. Lett.* **100**, 047209 (2008)
- [72] K. Nomura and N. Nagaosa, *Phys. Rev. Lett.* **106**, 166802 (2011)
- [73] J. G. Checkelsky, J. Ye, Y. Onose, Y. Iwasa, and Y. Tokura, *Nat. Phys.* **8**, 729 (2012)
- [74] H. Zhang, C.-X. Liu, X.-L. Qi, X. Dai, Z. Fang, and S.-C. Zhang, *Nat. Phys.* **5**, 438 (2009)
- [75] M. R. Mahani, A. Pertsova, M. F. Islam, and C. M. Canali, *Phys. Rev. B* **90**, 195441 (2014)
- [76] A. M. Black-Schaffer and D. Yudin, *Phys. Rev. B* **90**, 161413(R) (2014)
- [77] A. M. Black-Schaffer and A. V. Balatsky, *Phys. Rev. B* **85**, 121103 (2012)

reported in Fig. 2(d) in the main text. We also study whether the MAE is affected due to the inclusion of pair-wise interactions between Bi_{Se_1} . By using the same method as in the main text, we calculate the MAE per antisite defect and find it to be ~ 15 meV. This again is in close agreement with the values reported in the main text. Further, we use this setup to calculate the exchange coupling as the energy difference between the parallel (FM) and anti-parallel (AFM) configurations of the magnetic moments and find it to be 3.6 meV, as reported in the main text.

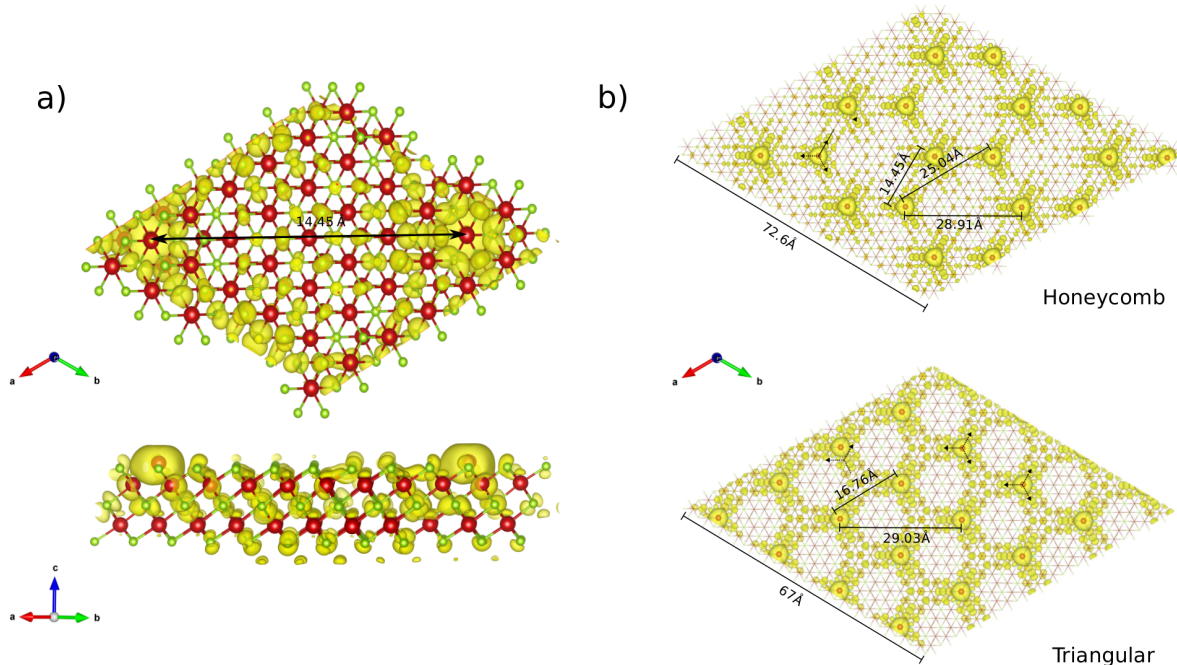


FIG. 2. (a) Real space magnetization density (iso-value 0.1 times the maximum) in a supercell with two Bi_{Se_1} defects at 6% concentration, with top (top) and side (bottom) views. (b) Triangular (top) and honeycomb (bottom) arrangements of Bi_{Se_1} antisite defects and their corresponding real-space magnetization densities. The three-fold (clover-leaf) magnetization for each Bi_{Se_1} , is schematically represented by three outward arrows.

We also comment on the atomic arrangement of the antisite defects. For the case of two Bi_{Se_1} in the supercell, discussed here in the Supplementary material, the antisite defects are arranged in a honeycomb lattice, as shown in fig. 2(b) (top). In contrast, for the case discussed in the main text, i.e. one Bi_{Se_1} per supercell, the antisite defects are arranged in a triangular lattice as shown in fig. 2(b) (bottom). Despite the differences, we find that the spontaneous magnetization and the MAE are similar, irrespective of the arrangements of the Bi_{Se_1} defects. To illustrate the spatial properties more clearly, we represent the spread of the three-fold (clover-leaf) magnetization with three out-ward arrows in fig. 2(b). We find that in the honeycomb arrangement the spread of the magnetization is such that the arrows belonging to one Bi_{Se_1} points in the direction of the other Bi_{Se_1} . While in the triangular case, the magnetization of each Bi_{Se_1} extends in such a way that the arrows point towards the center of the triangle formed by the antisite lattice. Based on these results, we conclude that the magnetization survives irrespective of its relative (between two Bi_{Se_1}) spread and hence should also not depend on the detailed arrangement on the defects, as long as the concentration of Bi_{Se_1} remains the same. This notably should make our results and conclusions insensitive to disorder effects.

Aligning the bands of defected and pristine Bi_2Se_3

In order to draw conclusions about the band structure of the antisite Bi_2Se_3 we need to properly align it with that of the pristine Bi_2Se_3 . In fig. 3 we plot the full band structure of both the pristine (red) and antisite (blue) slab following the alignment procedure described in the main text. For the defected system we plot the bands belonging to the bulk valence and conduction bands with dotted lines, while the states (defect and DSS) within the gap are shown with solid lines. We can easily make this distinction by noting their spatial extent within the slab. Clearly, we see that both the conduction and valence bands of both systems overlap essentially perfectly. This helps us to identify both the DSS and the defect states in the gap region.

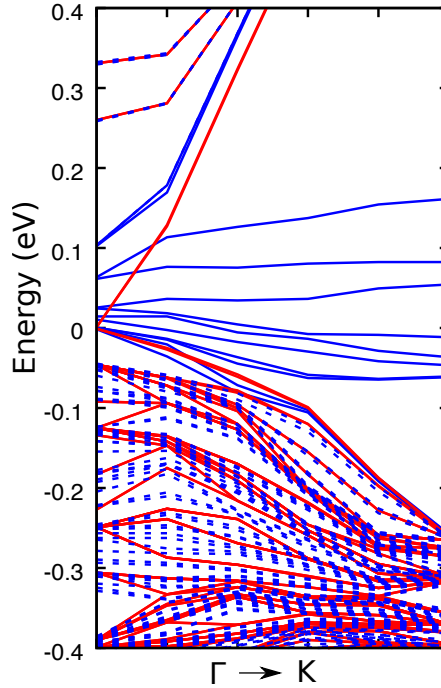


FIG. 3. Full band structure of the pristine (red) and defected (blue) slab with Bi_{Se_1} antisite defects. For the defected system, bulk bands are displayed with dashed lines. We align the pristine and defected bands such that the valence and conduction bands lie on top of each other.

Extracting the DSS for Bi_{Se_1} defects

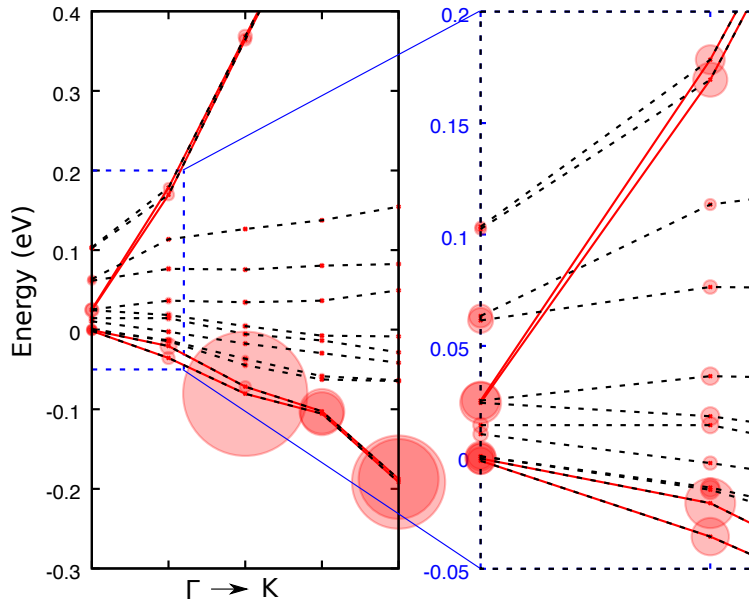


FIG. 4. Low-energy band structure of the Bi_{Se_1} antisite slab. The bands obtained by connecting the energy eigenvalues in a simple ascending order are shown in black-dotted lines. The diameter of the circles at each eigenvalue is set by the inverse of the orbital weight around the Bi_{Se_1} defect (see text). Larger circles thus correspond to less defect weight. The DSS bands (red) are obtained by connecting the largest circles at each k -point. To the right is an enlarged view of the region around the Γ -point, clearly displaying the energy gap and the finite hybridization between DSS and defect states.

Note that away from the Γ -point, we find that the DSS and the defect states are both well separated in energy and display large differences in circle diameters, demonstrating a very clear separation between the DSS and localized defect states. Closer the Γ -point we observe a notable hybridization between the DSS and the defect states. Here, circle diameters for the DSS states are only around three times larger than those of the defect states. Still, this difference makes it possible for us to unequivocally identify a finite energy gap, also consistent with the slope of the DSS. The hybridization in turn explains how the magnetization of the defect states can open up the energy gap as that provides the necessary coupling between the defect states and the DSS. In order to extract the DSS in the Bi_{Se_1} slab, we study the orbital weights for each low-energy eigenstate. For the purpose of displaying the data we sum the orbital weights for all atoms up to the next-neighbors (within a distance of 5 Å) of the Bi_{Se_1} defect. Then we use a circle at each energy eigenvalue, whose diameter is set by the inverse of this summed orbital weight, to display how much that particular eigenstate is delocalized over the whole surface, i.e., the larger the circle, the less localized defect character in that eigenstate. Doing this for all in-gap states, we can then connect those eigenvalues that have the largest circles to give the DSS as that is the state that is fully delocalized over the surface. The remaining bands are then identified as localized defect states. In fig. 4 we show the result, including a zoom-in around the Γ -point. We clearly observe the lower and upper branch of the DSS as they have significantly larger circles than the remaining states. They also show the characteristic linear dispersion as expected for a DSS.

Extracting the DSS for Bi_{Se_2} defects

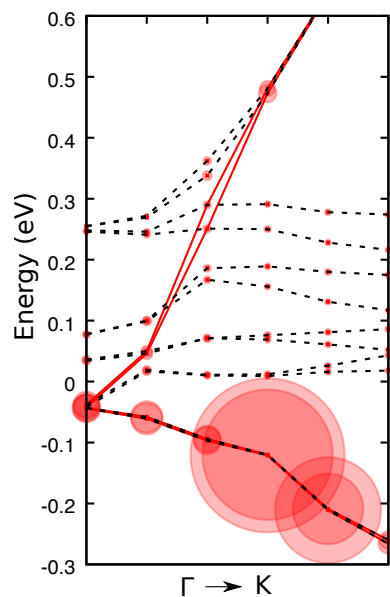


FIG. 5. Low-energy band structure of the Bi_{Se_2} antisite slab. The bands obtained by connecting the energy eigenvalues in the a simple ascending order are shown in black-dotted lines. The diameter of the circles at each eigenvalue is set by the inverse of the orbital weight around the Bi_{Se_2} defect (see text). Larger circles thus correspond to less defect weight. The DSS bands (red) are obtained by connecting the largest circles at each k -point.

We follow the same procedure as in the previous section also for the Bi_{Se_2} antisite defect slab and show the results in fig. 5. While there are large overall similarities with the Bi_{Se_1} system, we here find that the defect states are spread to higher energies. In particular, near the Γ -point, we find that the DSS do not hybridize with the defect states, simply because there are no defect states there. As a consequence, we also find no energy gap in the DSS. Far away from the Γ -point we however find some minor hybridization between the DSS and defect states, although that does not influence the properties around the Dirac point.

Comparing the (M)DOS of 6% and 25% concentrations and the Stoner mechanism

In the main text we attribute the spontaneous out-of-plane magnetization to the Stoner instability of the resonance peak near the Fermi level associated with Bi_{Se} . At the same time, in fig. 2(a,b) in the main text, we find that the magnetization and MAE show strong dependences on the concentration. Here, we clarify these differences in behavior

by comparing the resonance peaks for the antisite concentrations 6% and 25%. For this, we focus on how the peak width and the Stoner exchange splitting change with concentration.

In fig. 6 a (b) we show the DOS (MDOS) for both 6% and 25% concentrations of Bi_{Se_1} antisite defects. In order to look at how the peak width vary with concentration, we calculate the full width at half maxima (FWHM) of the resonance peaks find it to be 4.6 meV and 9.8 meV for 6% and 25% concentrations, respectively. Thus, we find that even for a significant increase in the concentration (from 6% to 25%), the peak-width only increases by a factor of 2. It is also interesting to note that the peak width is significantly smaller compared to other systems with spontaneous magnetization.^{1,2} This small peak width facilitates stability of the magnetic moments at high temperatures.³ However, we find that the Stoner exchange splitting is much more affected, see fig. 6(b) with an increase of the concentration from 6% to 25%. For the 6% case, we find an exchange splitting of 80 meV (strong ferromagnet), while for 25% we see that the splitting is just 6 meV (weak ferromagnet). Thus, we conclude that the exchange splitting depends strongly on the concentration, while the peak width is less affected. This clearly illustrates that, while both systems spontaneously magnetize, they show rather different magnetization properties.

Using the exchange splitting (E_{ex}) and the net magnetization (m) we can also roughly estimate⁴ the Coulumb interaction (U) by using the expression

$$U = \frac{E_{\text{ex}}}{m} \quad (1)$$

Thus, for 6% Bi_{Se} (which is the main focus in main text), we get $U = 93$ meV using this expression.

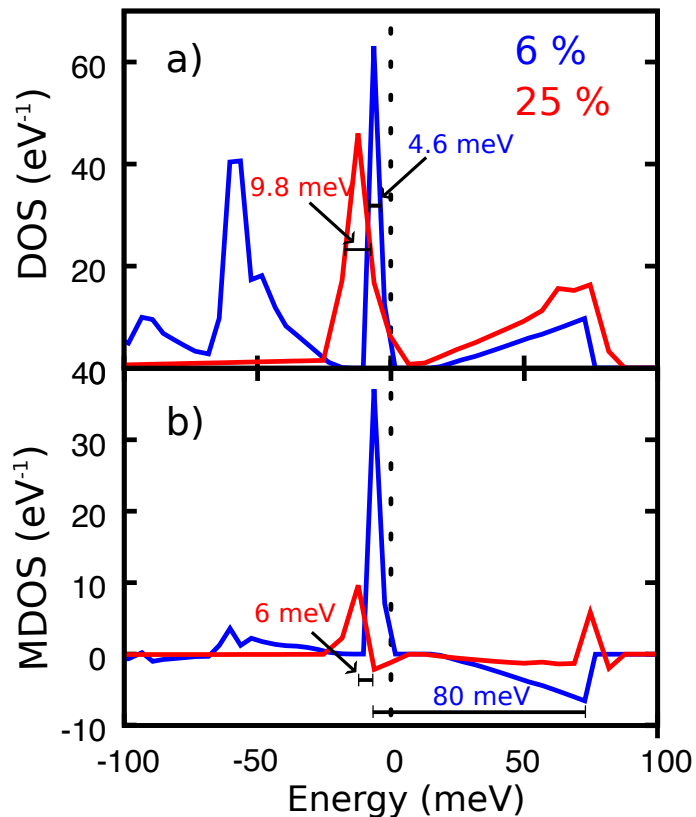


FIG. 6. a) DOS near the Fermi level for 6% (blue) and 25% (red) concentration of antisite defects Bi_{Se_1} , with full width at half maxima (FWWHM) indicated. b) MDOS near the Fermi level for 6% (blue) and 25% (red) concentration of antisite defects Bi_{Se_1} , with the Stoner exchange splitting energy indicated.

-
- ¹ X. Tang, L. Hu, T. Fan, L. Zhang, L. Zhu, H. Li, H. Liu, J. Liang, K. Wang, Z. Li, S. Ruan, Y. Zhang, D. Fan, W. Chen, Y.-J. Zeng, and H. Zhang, [Adv. Funct. Mater.](#) **29**, 1808746 (2019)
 - ² O. V. Yazyev and L. Helm, [Phys. Rev. B](#) **75**, 125408 (2007)
 - ³ D. M. Edwards and M. I. Katsnelson, [J. Phys.: Condens. Matter](#) **18**, 7209 (2006)
 - ⁴ R. Skomski, *Simple Models of Magnetism* (Oxford University Press, Oxford, 2008) Chap. Models of exchange